

Second Floor of Flatland: Epitaxial Growth of Graphene on Hexagonal Boron Nitride

Alexander Mehler, Nicolas Néel, Elena Voloshina, Yuriy Dedkov, and Jörg Kröger*

In the studies presented here, the subsequent growth of graphene on hexagonal boron nitride (h-BN) is achieved by the thermal decomposition of molecular precursors and the catalytic assistance of metal substrates. The epitaxial growth of h-BN on Pt(111) is followed by the deposition of a temporary Pt film that acts as a catalyst for the fabrication of the graphene sheet. After intercalation of the intermediate Pt film underneath the boron-nitride mesh, graphene resides on top of h-BN. Scanning tunneling microscopy and density functional calculations reveal that the moiré pattern of the van-der-Waals-coupled double layer is due to the interface of h-BN and Pt(111). While on Pt(111) the graphene honeycomb unit cells uniformly appear as depressions using a clean metal tip for imaging, on h-BN they are arranged in a honeycomb lattice where six protruding unit cells enframe a topographically dark cell. This superstructure is most clearly observed at small probe–surface distances. Spatially resolved inelastic electron tunneling spectroscopy enables the detection of a previously predicted acoustic hybrid phonon of the stacked materials. Its spectroscopic signature is visible in surface regions where the single graphene sheet on Pt(111) transitions into the top layer of the stacking.

metries and concomitant functionalities.^[1] Electronic and optical^[2–5] as well as magnetic^[6–10] properties associated with van-der-Waals-coupled layers were reported.

The combination of graphene on hexagonal boron nitride (h-BN) is a particularly interesting stacking of 2D materials.^[11,12] Using h-BN as a supporting substrate for graphene has several advantages compared to graphene on SiO₂, which represents the most commonly used substrate for graphene devices to date.^[13–16] The inertness of h-BN together with the absence of dangling bonds, which both are favored by the strong ionic in-plane B–N bonds, are supposed to help decouple graphene very efficiently from the environment and, thus, retain its genuine properties. Indeed, the graphene–h-BN stacking revealed improvements in the graphene electron mobility,^[11] fractional quantum Hall effect,^[17] and in the ballistic charge transport.^[18]

1. Introduction

The stacking of 2D materials, which are coupled by the weak van der Waals interaction, is attracting increasing interest. Owing to their low mutual hybridization rotational and translational degrees of freedom allow the control of distinct stacking sym-


The preparation of graphene on h-BN, however, represents an experimental challenge. Very often, the heterostructure is fabricated by transferring graphene—chemically grown or exfoliated—onto h-BN. This transfer procedure may lead to pronounced graphene rippling and trapped contaminants residing at the graphene–h-BN interface.^[19] Alternative routes to the growth of graphene on h-BN were reported previously, such as chemical vapor deposition (CVD).^[20–26] In many cases, CVD proceeds via the thermal decomposition of molecular precursors, which is facilitated by the catalytic activity of a metal surface. At the same time, a minimal residual coupling of the individual 2D layers with the metal is most desirable in order to retain a quasi-free state of the adsorbed 2D materials. The residual hybridization of graphene on h-BN with some metals, such as Ni, hampers the preservation of the unique free-state properties. The additional intercalation of Au was previously suggested to more efficiently decouple graphene from a h-BN-covered Ni(111) film grown on W(110).^[27] A more general class of substrates serving as hosts for the stacking became accessible by plasma-enhanced CVD.^[28,29]

In the work presented here the fabrication of graphene atop h-BN on Pt(111) on the basis of the thermal decomposition of molecular precursors and the catalytic assistance of the metal substrate is reported, which so far has successfully been applied to the growth of bilayer graphene.^[30] The combination of STM and density functional calculations shows that the resulting moiré pattern of the graphene–h-BN stacking is due to the

A. Mehler, N. Néel, J. Kröger
Institut für Physik
Technische Universität Ilmenau
D-98693 Ilmenau, Germany
E-mail: joerg.kroeger@tu-ilmenau.de

E. Voloshina, Y. Dedkov
Physics Department
Shanghai University
Shanghai 200444, P. R. China

E. Voloshina, Y. Dedkov
Institut für Chemie und Biochemie
Freie Universität Berlin
D-14195 Berlin, Germany

 The ORCID identification number(s) for the author(s) of this article can be found under <https://doi.org/10.1002/smll.202102747>.

© 2021 The Authors. Small published by Wiley-VCH GmbH. This is an open access article under the terms of the Creative Commons Attribution License, which permits use, distribution and reproduction in any medium, provided the original work is properly cited.

DOI: 10.1002/smll.202102747

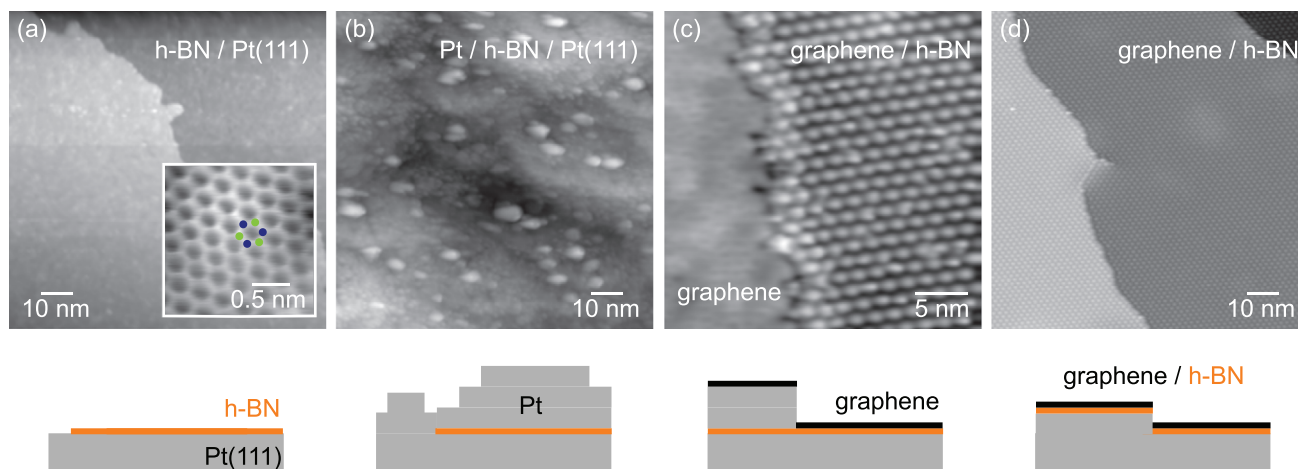


Figure 1. Preparation of graphene on h-BN. a) STM image of a single h-BN layer on Pt(111) (bias voltage: 2.4 V, tunneling current: 100 pA, size: 100 nm \times 100 nm). Inset: Atomically resolved h-BN lattice with indicated positions of B and N (10 mV, 600 nA, 2 nm \times 2 nm). b) STM image of h-BN-covered Pt(111) after deposition of a Pt film (1.15 V, 100 pA, 100 nm \times 100 nm). Compact protrusions are due to Pt clusters residing on the closed metal film. c) STM image of a surface region where the graphene-covered Pt film (left) is juxtaposed to the graphene-h-BN stacking (right) by a Pt film step edge (0.5 V, 100 pA, 30 nm \times 30 nm). d) STM data for the graphene-h-BN stacking on Pt(111) (1 V, 100 pA, 100 nm \times 100 nm). The sketches under the STM images in (a-d) represent side views of the suggested stackings.

h-BN-Pt(111) interface. At small probe-surface distances, STM images show that the graphene-h-BN heterostructure in addition to the moiré lattice exhibits a honeycomb superstructure. The stacking was further characterized by inelastic electron tunneling spectroscopy (IETS). A predicted acoustic hybrid phonon of the graphene-h-BN stacking leaves its fingerprint in spectra of the differential conductance (dI/dV) atop surface regions where the single graphene layer on Pt(111) transitions into the top layer of the graphene-h-BN stacking. Sufficiently far from the transition zones, the graphene-h-BN stacking as well as monolayer graphene (MLG) on Pt(111) remain featureless in IETS. The latter observation together with the additional graphene honeycomb superstructure hint at a finite graphene-surface coupling, which contrasts expectations of a quasi-free state of graphene on h-BN.

2. Results and Discussion

2.1. Fabrication of the Graphene-h-BN Stacking and Its Moiré Pattern

The use of Pt as a metal substrate is motivated by two advantages. First, the Pt substrate acts as a catalyst for the growth of h-BN on Pt(111) in the initial step of the growth procedure. The Pt film deposited on h-BN in the subsequent step then serves as the catalytically active metal substrate for graphene growth. Second, the h-BN-Pt(111) hybridization is weak,^[31] which is supposed to favor a reduced residual graphene-Pt(111) coupling, too. Furthermore, the catalytically assisted thermal decomposition of molecular precursors—BNH₆ for h-BN and C₂H₄ for graphene—guarantees a self-limiting growth process for h-BN^[32–36] and graphene,^[37–39] that is, the number of the individual 2D layers is restricted to one in each of the subsequent preparation steps.

Figure 1 shows STM images of the surface that were acquired after individual steps of the preparation of the graphene-h-BN stacking on Pt(111). The fabrication of h-BN on Pt(111) from

molecular precursor BNH₆ leads to a closed sheet that extends over several terraces (Figure 1a), in agreement with previous works.^[31,40,41] The subsequent deposition of the Pt film gives rise to a strongly corrugated surface, which is due to Pt clusters residing on a closed Pt film (Figure 1b). At the film-h-BN interface an epitaxial relationship between the Pt film and h-BN likely applies, as observed for Au deposition on h-BN^[42] or for Pt on graphene.^[43] Due to strain relief with increasing film thickness, this possible epitaxial relationship may be lost, however. A sufficiently thick film—30 to 50 atomic layers—is needed for the preparation of graphene by the thermal decomposition of C₂H₄. The required annealing of the sample in the process of graphene formation concomitantly induces the efficient Pt intercalation through h-BN, which in case of too thin a Pt film reduces the catalytically active surface regions. Test experiments revealed that annealing of the Pt-covered h-BN-Pt(111) sample at 1170 K for 20 min results in an entirely intercalated Pt film (see Figure S1, Supporting Information). Figure 1c presents an STM image that was directly acquired after graphene growth on the Pt film. Most obvious is a periodic array of protrusions in the right part of the STM image; its period is \approx 1.65 nm. As will be scrutinized below, this array reflects a moiré pattern that is due to the h-BN-Pt(111) interface. From similar STM data with atomic resolution (see below) the presence of graphene covering the entire probed surface region in Figure 1c can be inferred. Therefore, the left part of the STM image in Figure 1c shows graphene on the residual Pt deposit. Additional annealing produces a laterally extended graphene-h-BN stacking (Figure 1d) with the moiré lattice of Figure 1c visible on all terraces. Average lateral extensions of the stacking exceed 150 nm \times 150 nm. The large-scale quality of the stacking also reflects that the intercalated Pt film grew in the expected layer-by-layer manner with (111) orientation, as reported for the Pt deposition on pristine Pt(111) at elevated temperature.^[44,45]

Before analyzing the moiré pattern of the graphene-h-BN stacking in more detail, the actual presence of the stacking

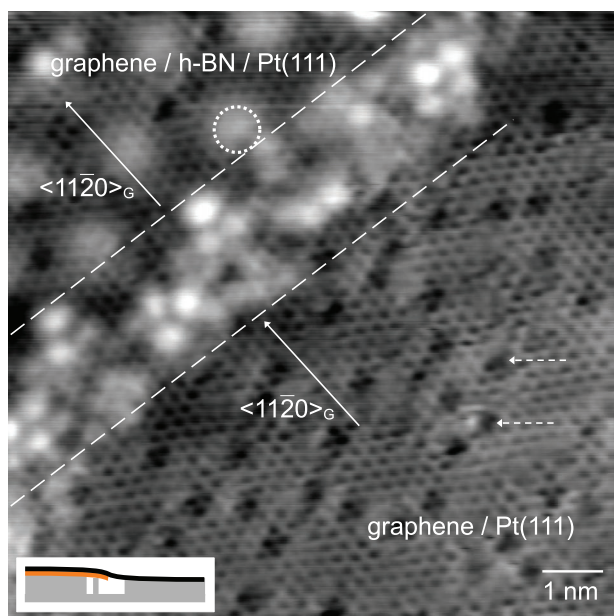


Figure 2. STM image of graphene (lower right) and graphene on h-BN (upper left) (100 mV, 200 pA, 10 nm × 10 nm). The intercalated Pt film has adopted a (111) orientation. The graphene honeycomb lattice is resolved in both surface regions that are separated by a transition zone within the two parallel dashed lines. A crystallographic direction of graphene is indicated. The dashed arrows point at two of the multiple Pt(111) surface defects. A mound of the moiré pattern visible on the graphene–h-BN stacking is marked by a dashed circle. Inset: Suggested stacking geometry where the top graphene sheet covers both h-BN (left) and the Pt surface (right).

and its order-graphene on top of h-BN is clarified. To this end, **Figure 2** shows a representative STM image of a surface region where—presumably—MLG on Pt(111) (lower right part of the STM image) transitions into the graphene–h-BN stacking (upper left part). The atomic resolution was achieved owing to the accidental termination of the tip apex with a surface impurity. The transition region, which is approximately confined between the pair of parallel dashed lines in **Figure 2**, is characterized by an irregular arrangement of protrusions. Most likely, these structures are due to residual intercalated Pt atoms or clusters. Importantly, in agreement with previous reports^[30,39,41,46] a moiré pattern is absent from the lower right part of the STM image, which strongly hints at graphene rather than h-BN as the imaged 2D material because h-BN-covered Pt(111) gives rise to a clearly discernible moiré lattice (see **Figure S2**, Supporting Information). Indeed, the absence of a moiré pattern is consistent with the weak graphene–Pt(111) hybridization^[47] and large twist angles enclosed by the close-packed lattice direction of graphene, $\langle 11\bar{2}0 \rangle_G$, and Pt(111), $\langle 1\bar{1}0 \rangle$,^[39,46] as inferred from the atomically resolved graphene (**Figure 2**) and Pt(111) (see **Figure S3**, Supporting Information) lattices. The enclosed angle in the present case is $\varphi_{G,Pt} \equiv \angle(\langle 11\bar{2}0 \rangle_G, \langle 1\bar{1}0 \rangle) = 12^\circ \pm 2^\circ$. In addition, spectroscopy of dI/dV performed atop the monolayer is indicative of graphene (see **Figure S4**, Supporting Information). Furthermore, hydrocarbon molecules adsorbed on these surface regions exhibit signatures of Franck–Condon vibrons that are characteristic for graphene (see **Figure S5**, Supporting Information) and clearly deviate from the situation on h-BN.^[41]

Therefore, the presence of MLG on Pt(111) after the subsequent growth of h-BN and graphene can reasonably be assumed.

Graphene remains the top layer in stacking regions of the surface, which can be inferred from **Figure 2** as well. It is obvious from the STM image that irrespective of the transition, the graphene sheet continuously covers the entire surface area and retains its orientation. The occurrence of the moiré pattern (**Figure 1c,d**) in the upper left part of the STM image in **Figure 2** hints at the presence of a bilayer stacking. Furthermore, defect sites of the Pt(111) surface that appear as faint depressions in STM images of MLG-covered Pt(111) (dashed arrows in **Figure 2**) are suppressed in surface regions where the moiré pattern occurs. Therefore, one may reasonably conclude that a bilayer stacking is present on the surface and that the top 2D material is graphene. The preparation method strongly lends support to h-BN presenting the bottom layer of the stacking. The calculations to be discussed next indeed demonstrate that the moiré pattern is due to the h-BN–Pt(111) interface and, thereby, further corroborate that the bilayer stacking is graphene on h-BN. Moreover, the IETS experiments that will be presented in the following section are compatible with the excitation of a graphene–h-BN hybrid phonon and likewise reveal the presence of the heterostacking.

Next, the moiré pattern visible in **Figure 1c,d** will be analyzed and its origin identified. To this end, **Figure 3** presents a cascade of typical STM images of the same stacking surface region as a function of increasing tunneling current, that is, of decreasing tip–surface distance. At low current (**Figure 3a**) the main moiré lattice, referred to as *M* hereafter, is spanned by unit cell vectors \mathbf{m}_1 and \mathbf{m}_2 with $m \equiv |\mathbf{m}_1| = |\mathbf{m}_2| = 1.65 \pm 0.04$ nm. The atomically resolved graphene lattice atop h-BN (**Figure 2**) unravels the angle $\varphi_{M,G} \equiv \angle(\mathbf{m}_1, \langle 11\bar{2}0 \rangle_G) = 5^\circ \pm 2^\circ$. Increasing the tunneling current (**Figure 3b–d**) yields an additional superstructure that gradually appears in the STM images and will be referred to as *A*. The individual C atom honeycomb cells arrange themselves in a honeycomb superlattice where a diamond unit cell spanned by vectors $\mathbf{a}_1, \mathbf{a}_2$ (**Figure 3d**) contains two C honeycomb cells that appear as protrusions in STM images (red dots in **Figure 3e**) and one C honeycomb cell that appears as a depression. The analysis of a multitude of STM images yields $|\mathbf{a}_1| = |\mathbf{a}_2| = 0.45 \pm 0.03$ nm $\approx \sqrt{3}g$ (*g*: lattice constant of graphene) and $\angle(\mathbf{a}_1, \langle 11\bar{2}0 \rangle_G) = 30^\circ \pm 1^\circ$. Therefore, the honeycomb superstructure may be described as $(\sqrt{3} \times \sqrt{3})R30^\circ$ with respect to the graphene lattice spanned by $\mathbf{g}_1, \mathbf{g}_2$ (**Figure 3e**).

It is tempting to trace *M* to the twist angle enclosed by graphene and h-BN lattices, $\varphi_{G,h-BN} \equiv \angle(\langle 11\bar{2}0 \rangle_G, \langle 11\bar{2}0 \rangle_{h-BN})$. Twist angles $\varphi_{G,h-BN} = \pm 8.5^\circ$ can reproduce the experimentally observed spatial period of *M*, $m \approx 1.65$ nm. However, the angle between this modeled moiré lattice and $\langle 11\bar{2}0 \rangle_G$ is $\varphi_{M,G} \approx \mp 20^\circ \neq \varphi_{M,G}$. Furthermore, a moiré superstructure due to the twist of graphene with respect to Pt(111) can likewise be excluded. Using the measured twist angle $\varphi_{G,Pt} \approx 12^\circ$ leads to a moiré lattice constant of ≈ 0.65 nm, which deviates clearly from *m* (see **Figure S6**, Supporting Information). Therefore, in order to account for the origin of *M* it is necessary to resort to the h-BN–Pt(111) interface. Using twist angles $\varphi_{h-BN,Pt} \equiv \angle(\langle 11\bar{2}0 \rangle_{h-BN}, \langle 1\bar{1}0 \rangle) = \pm 7^\circ$ a spatial period of ≈ 1.65 nm is obtained. The known $\langle 1\bar{1}0 \rangle$ direction of Pt(111) (see **Figure S3**, Supporting Information) requires to set $\varphi_{h-BN,Pt} = -7^\circ$ (see **Figure S6**, Supporting Information).

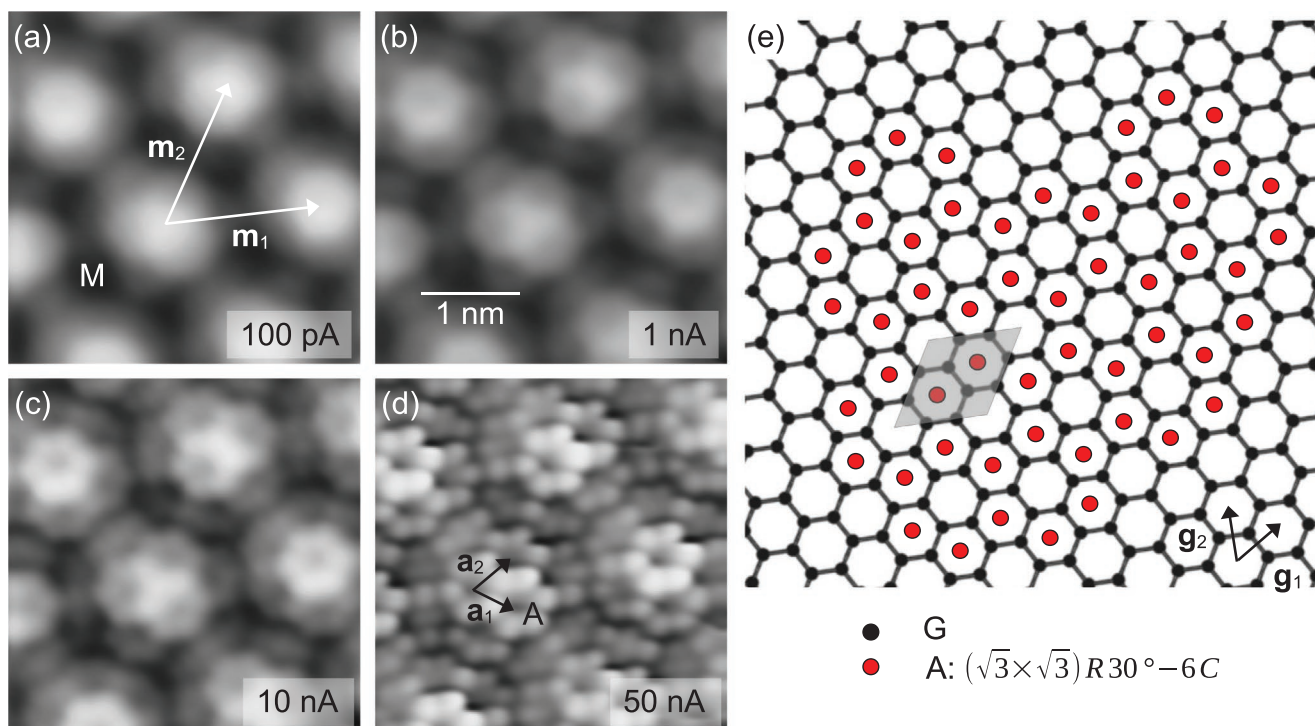


Figure 3. Moiré pattern of graphene–h-BN on Pt(111). a) STM image (10 mV, 100 pA, 3.6 nm × 3.6 nm) with \mathbf{m}_1 , \mathbf{m}_2 spanning the unit cell of the moiré lattice M . b–d) STM images of the same surface region as in (a) with increasing tunneling current. The additional superstructure A is spanned by \mathbf{a}_1 , \mathbf{a}_2 . e) Graphene lattice spanned by \mathbf{g}_1 , \mathbf{g}_2 . Red dots indicate the honeycomb array of protrusions visible in STM images at elevated current. The diamond unit cell of superstructure A contains 6 C atoms. The scale bar depicted in (b) applies to (a,c,d) as well.

Before presenting the calculated results it is worth mentioning that a nearly uniform graphene orientation was observed across all explored surface regions. For different stacking domains the h-BN–Pt(111) moiré lattice orientation varies by $\approx 7^\circ$, which is compatible with changes of not more than 1° in the twist angle enclosed by h-BN and Pt(111) lattices. These observations indicate that graphene growth atop h-BN forces a particular orientation of the h-BN layer. Without graphene, h-BN is known to grow on Pt(111) with alignment of the crystallographic orientations.^[40,48]

For the density functional calculations the experimentally obtained geometric data served as initial input parameters. **Figure 4a** summarizes the structural model inferred from observed data such as the $\langle 1\bar{1}0 \rangle$ direction of Pt(111), the twist angles $\varphi_{\text{h-BN, Pt}} = -7^\circ$ and $\varphi_{\text{G, Pt}} = 12^\circ$. A simulated STM image based on calculated charge densities (see Figure S7, Supporting Information) of the stacking with relaxed atom positions is presented in Figure 4b. The spatial period and the orientation of the moiré lattice are in agreement with the experimental data (Figure 4c). Given the complexity of the stacking of two different 2D materials on a metal surface the degree of agreement represents a notable achievement. The accordance of the two data sets is further corroborated by comparing cross-sectional profiles (see Figure S8, Supporting Information). According to the simulations, the bright moiré mound regions in STM images correspond to sites where N and B atoms reside above top and fcc hollow sites of the Pt(111) lattice, respectively. Since the involved orbitals overlap effectively at these sites, the

main STM contrast is governed by the charge distribution at the h-BN–Pt(111) interface. The contrast is additionally modulated by the electron density at C atoms of the graphene lattice (see Figure S9, Supporting Information).

The 2D Fourier transforms of calculated and experimental STM images depicted in Figure 4d,e deviate from each other. While M and graphene lattices are well reproduced by the simulations, the calculations reveal a superstructure M' that is not visible in the Fourier transform of the experimental STM image (Figure 4e). In direct space, M' yields a spatial period of ≈ 0.75 nm and a twist angle $\varphi_{M',G} \approx 16^\circ$ with respect to $\langle 11\bar{2}0 \rangle_G$. These values are compatible with a moiré pattern resulting from twisted graphene and h-BN lattices with $\varphi_{\text{G, h-BN}} = 19^\circ$ (Figure 4a). STM images recorded at elevated current are dominated by the strongly corrugated A , M and graphene lattices, which can explain the absence of M' from experimental data due to its low buckling. Topographic data acquired at low tunneling currents where superstructure A and the graphene lattice are efficiently suppressed indeed show an additional superlattice, which is consistent with twisted graphene and h-BN meshes (see Figure S10, Supporting Information).

While the overall agreement of simulations and experimental data with regard to the bilayer stacking of two different 2D materials on a metal surface is very good, the complexity of the stacking—graphene on h-BN on Pt(111)—is difficult to match in the density functional calculations. In particular, the finite unit cell underlying the calculations (see Figure S7, Supporting Information) is an approximation to the experimental

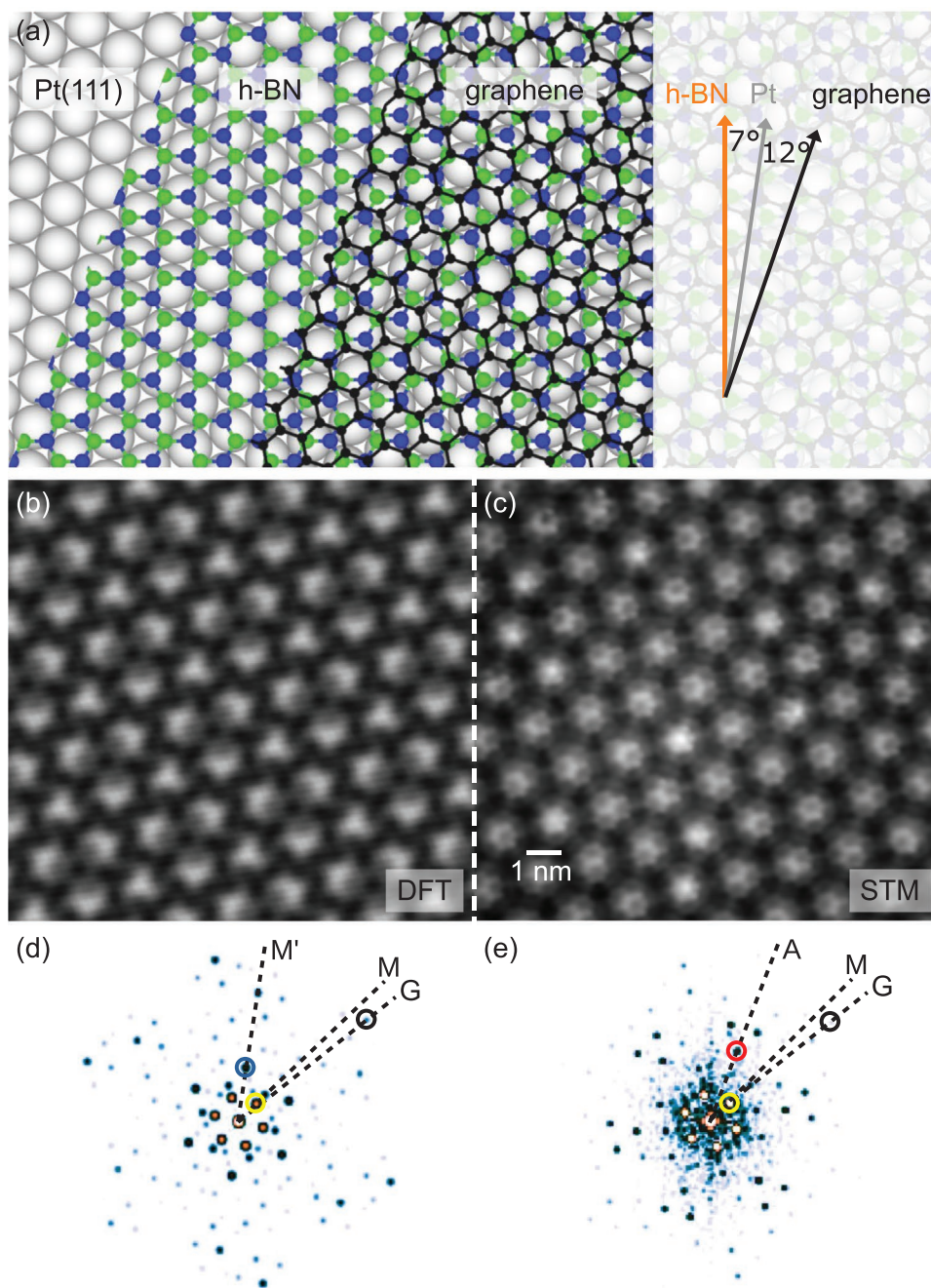


Figure 4. Comparison of calculated and experimental STM data. a) Suggestion of stacking geometry on the basis of experimental data. b) Calculated STM image (50 mV, 12.7 nm × 13.5 nm). c) Experimental STM image (10 mV, 200 nA, 12.7 nm × 13.5 nm). The depicted scale bar applies to (b), too. d) Fourier transform of data shown in (b) with indicated (dashed lines) directions of graphene, *M* and *M'* lattices. e) Fourier transform of data shown in (c) with indicated (dashed lines) directions of graphene, *M* and *A* lattices.

situation and, therefore, can lead to missing superstructures, such as *A*. The origin of *A* remains elusive. It is not related to the geometry of the stacking alone; that is, a recurring stacking sequence of atoms with the regularity of superstructure *A* is missing. In addition, relaxations of the 2D lattices are unlikely due to the low charge transfer between Pt(111) and h-BN as well as between h-BN and graphene (see Figure S7, Supporting Information). Moreover, trapping of Pt atoms at the

graphene–h-BN or h-BN–Pt(111) interface in the course of intercalation is unlikely, too, in view of the extended annealing at elevated temperature. The electronic structure of the stacking remains as a reasonable origin of the superstructure. Because structure *A* becomes most clearly visible at small tip–graphene distance, electronic wave functions that are confined to the graphene plane appear to play an important role in the occurrence of *A*.

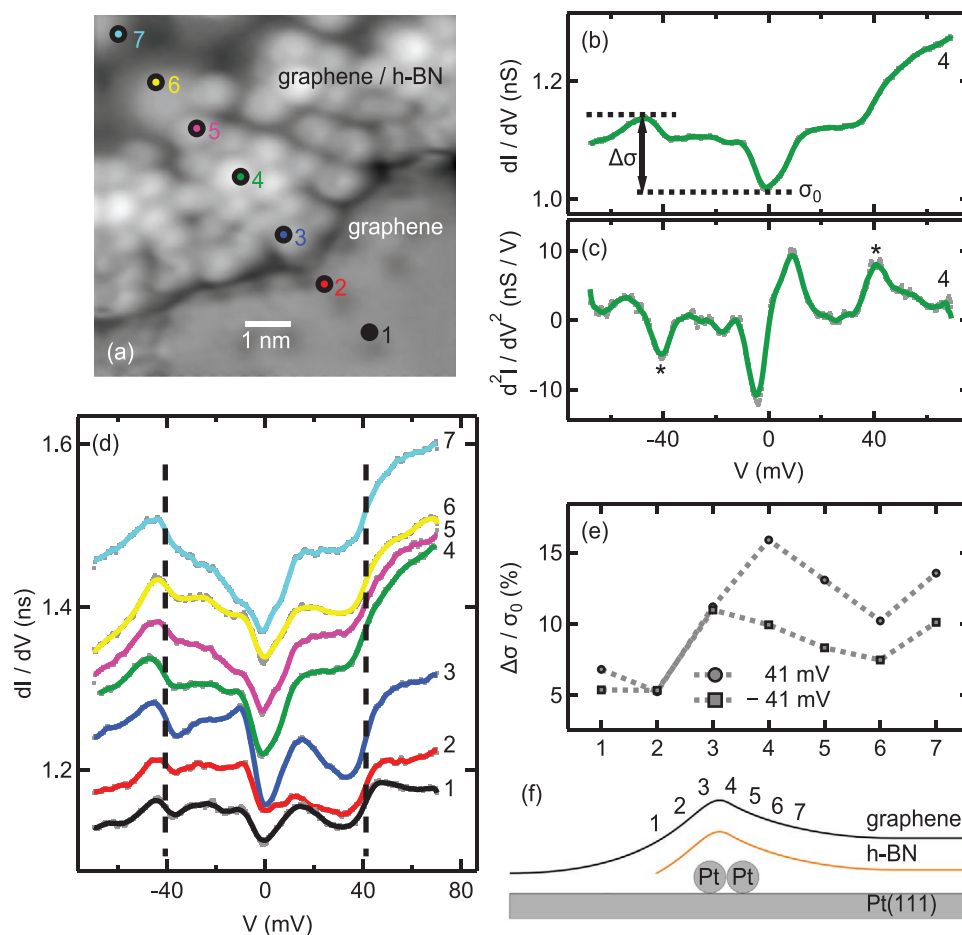


Figure 5. Phonon spectroscopy on the graphene–h-BN stacking. a) STM image of a surface region where graphene on Pt(111) (lower right) transitions into graphene on h-BN (upper left) (70 mV, 100 pA, 8 nm × 8 nm). Dots and numbers mark spectroscopy sites. b) Spectrum of dI/dV recorded above site 4 indicated in (a). $\Delta\sigma$ is defined as the change in dI/dV due to phonon excitation with respect to $\sigma_0 = dI/dV(V = 0V)$. c) Spectrum of d^2I/dV^2 recorded atop site 4. d) Spatially resolved dI/dV spectra acquired at sites 1–7 marked in (a). Spectra 2–7 are vertically offset. Dashed lines indicate inelastic excitations at $\approx\pm 41$ mV. In (b–d) raw data appear as dots and smoothed data as solid lines. Feedback loop parameters for (b–d): 70 mV, 100 pA. e) Evolution of $\Delta\sigma/\sigma_0$ at -41 mV (squares) and 41 mV (dots) with the spectroscopy site. f) Sketched side view of suggested transition of MLG on Pt(111) into stacked graphene on h-BN with indicated spectroscopy positions.

2.2. Phonon Excitations

The significance of the phonon spectroscopy experiments to be presented next is twofold. First, the excitation of a hybrid graphene–h-BN phonon in IETS additionally corroborates the successful fabrication of the desired heterostacking. Second, more fundamentally, owing to the presumably weak hybridization of the heterostacking with the Pt(111) surface the injected electron (or hole) is expected to efficiently couple to the phonon degrees of freedom of the stacking before it relaxes to the metal. Therefore, strong IETS signals should be measured, as observed for example, for graphene on SiC,^[49] SiO₂,^[15,50] h-BN-covered SiO₂,^[51,52] delaminated graphene nanostructures on Pt(111),^[53] Ir(111),^[54] and alkali-metal-intercalated graphene on Ir(111).^[55,56]

Several surprising observations for graphene on h-BN-covered Pt(111) are reported here, however. **Figure 5a** shows an STM image where graphene on Pt(111) (lower part of the STM image) transitions into the graphene–h-BN stacking (upper part), similar to **Figure 2** without resolution of the graphene

honeycomb mesh. Spatially resolved dI/dV and d^2I/dV^2 spectra were acquired atop the indicated positions 1–7. Representative examples of such spectra are displayed in **Figure 5b,c**. As most clearly seen in the d^2I/dV^2 data a dip-peak pair, which is symmetrically positioned around zero bias voltage is observed at ≈ -41 mV (dip) and ≈ 41 mV (peak), both marked with an asterisk. This dip-peak pair is assigned to a phonon excitation. All other features exhibit bias voltages that are not symmetric with respect to zero bias voltage and are not attributed to inelastic excitations.

The signature at $\approx\pm 41$ mV is common to all spatially resolved dI/dV spectra (**Figure 5d**) with varying signal strength. Spectra acquired ≈ 5 nm away to either side of the transition region, that is, on the stacking as well as on MLG, do not exhibit inelastic signatures (see **Figure S4**, Supporting Information). The signal strength is evaluated as the ratio $\Delta\sigma/\sigma_0$ (**Figure 5b**), which adopts $\approx 5\%$ on graphene-covered Pt(111) close to the transition zone and exceeds 15% atop the transition region (**Figure 5e**). The relative changes in dI/dV due to phonon excitation are

similar to the changes reported from IETS experiments on graphene-covered h-BN on SiO₂.^[51,52] The extracted phonon energy of ≈41 meV, however, does not match the reported values.^[51,52] Moreover, this energy is not compatible with flat dispersion branches and, thus, high phonon density of states (DOS) of free^[57] or quasi-free^[58–61] graphene.

Two possible scenarios may resolve these conflicting observations. The first scenario attributes a hybrid graphene–h-BN phonon to the spectral signatures at ≈±41 mV. A previous calculation showed that a hybrid out-of-plane acoustic phonon mode exhibits a nearly horizontal dispersion and, thus, high phonon DOS along a symmetry direction of the Brillouin zone (BZ) with an energy of 299.8 cm⁻¹ ≈ 37 meV.^[62] Moreover, in gated planar tunneling junctions comprising a graphene–h-BN stacking, the so-called K₆ phonon appeared at ≈46 mV in IETS and was assigned to a graphene–h-BN hybrid phonon, too.^[63] The deviation from the previously reported energies^[62,63] may be caused by different twist angles. While the calculations were performed for the graphene–h-BN Bernal stacking^[62] and the planar tunneling studies were carried out for the AA stacking sequence of graphene on h-BN,^[63] the experimentally inferred twist angle between the 2D materials reported here is 19° ± 2° (Figure 4a). Indeed, a dependence of graphene phonon energies on the twist angle was demonstrated for bilayer graphene.^[64,65]

The second scenario reflects a possible impact of the ($\sqrt{3} \times \sqrt{3}$)R30° superstructure on the phonon dispersion. Back-folding effects may distort the dispersion relation of, for example, the out-of-plane acoustic phonon of graphene along the Γ K and Γ M direction of the BZ (see Figure S11, Supporting Information). This scenario does not necessarily require the presence of a graphene–h-BN hybrid phonon.

The observation that phonon signals only occur in the spectra recorded atop the transition region while they fall below the detection limit sufficiently far away from it (≈5 nm to either side) provides a hint to a possible stacking configuration in the transition region (Figure 5f) and a preference to the applicability of the first scenario, which favors the presence of a hybrid phonon mode in IETS. Residual Pt intercalants, which can be Pt atoms or clusters, detach graphene and h-BN from the Pt(111) surface. The concomitant reduction of the hybridization with the metal substrate is most likely the reason for the phonon signature appearing in IETS. Previously, graphene blisters and wrinkles that were partly delaminated from Pt(111) and Ir(111) surfaces were reported to yield appreciable graphene phonon signals.^[53,54] The illustration of the stacking in Figure 5f also explains that the observation of phonon excitation in spectra 1 and 2 are compatible with a hybrid graphene–h-BN phonon. While the graphene–h-BN stacking is already present on the left side of the intercalant (Figure 5f, positions 1 and 2 in Figure 5a) the characteristic moiré pattern is not visible in STM images because of the elevated interface width between h-BN and Pt(111). This interpretation includes that the graphene–h-BN stacking well apart from the transition region exhibits a residual hybridization with the Pt(111) surface that is strong enough to impede the efficient excitation of phonons. A previous work demonstrated that the signal strength in IETS reflects the balance between elastic and inelastic electron transport channels whose transmissions are determined by the hybridization of the 2D material with the metal electrodes.^[55,56]

The transmission of the elastic transport channel increases with increasing coupling of the 2D material to the metal substrate, which concomitantly reduces the relative contribution of the inelastic transport channel in IETS. Therefore, the spectroscopic results presented here support the idea that the graphene–h-BN stacking on Pt(111) is not in its quasi-free state, in contrast to expectations. It will be interesting to explore whether the quasi-free state can be approached by different sets of twist angles.

3. Conclusion

The subsequent epitaxial growth of laterally extended graphene on h-BN by means of the catalyst-assisted thermal decomposition of molecular precursors has been achieved on Pt(111) and a temporarily intermediate Pt film. The growth process benefits from the catalytic activity of both the single-crystalline metal surface at the start of the growth process and the deposited metal film prior to growth of the second 2D material. Furthermore, the self-limiting growth controls the number of layers—one h-BN sheet residing beneath one graphene sheet. While the presented method has successfully been used to prepare laterally extended stacking regions of graphene on h-BN-covered Pt(111) with a high degree of crystallinity, the fabrication of other 2D stackings falls into the realm of the preparation protocol. Moreover, different substrate materials are likely to be applicable in place of Pt. Accompanying density functional calculations are important to identify the origin of moiré patterns and to explain the contrast formation in STM images, which give valuable insight into the actual stacking geometry. A hybrid graphene–h-BN acoustic phonon appears in IETS only in surface regions where the stacking is partly delaminated from the metal surface due to residual intercalant clusters. Consequently, the local vibrational spectroscopy of graphene on h-BN-covered Pt(111) exhibits a finite residual hybridization with the surface, in contradiction to common expectations.

4. Experimental Section

Experiment: The experiments were performed with an STM operated at 5 K and in ultrahigh vacuum (10⁻⁹ Pa). Surfaces of Pt(111) were prepared by repeated Ar⁺ bombardment and annealing (1400 K) in an O₂ atmosphere (4 × 10⁻⁵ Pa). Ammonia borane (BNH₆, purity 97%) was sublimated from a heated Ta crucible and deposited onto clean Pt(111) at room temperature. Annealing at 1200 K yielded a single layer of h-BN owing to self-limiting growth.^[32–36] The Pt film was subsequently grown by exposing the h-BN-covered surface to a Pt atom flux resulting from a partly sublimated Pt wire (purity 99.99%) wrapped around a resistively heated W filament. The film thickness was estimated by readings of a quartz balance in combination with STM images of submonolayer Pt coverage as 30 to 50 atomic layers. Graphene was then prepared on this film by the thermal decomposition of ethylene (C₂H₄, 4 × 10⁻⁵ Pa, purity 99.9%) at 1200 K. The entire intercalation of the Pt film was achieved by the additional annealing of the sample at 1200 K. STM images were recorded at constant current with the bias voltage applied to the sample and processed with WSxM.^[66] Spectroscopy of dI/dV and of d²I/dV² proceeded by sinusoidally modulating (5 mV_{rms}, 754 Hz) the bias voltage and measuring the, respectively, first and second harmonic of the current response of the tunneling junction with a lock-in amplifier.

Theory: Density functional calculations based on plane-wave basis sets of 400 eV cutoff energy were performed with the Vienna ab initio simulation package.^[67,68] The Perdew–Burke–Ernzerhof exchange–correlation functional^[69] was employed. The electron–ion interaction was described within the projector augmented wave method^[70] with C (2s, 2p), B (2s, 2p), N (2s, 2p) and Pt (5d, 6s) states treated as valence states. The BZ integration was performed on Γ -centered symmetry-reduced Monkhorst–Pack meshes using a Methfessel–Paxton smearing method of first order with $\sigma = 0.2$ eV. The k mesh for sampling the supercell BZ was chosen to be as dense as 3×3 . Dispersion interactions were considered by adding a $1/r^6$ atom–atom term as parametrized by Grimme.^[71] The system studied in the present work was considered in the supercell geometry due to the relative lattice size mismatch between graphene and the underlying metal. This supercell was constructed from a slab of four metal layers, a h-BN and graphene layer adsorbed on one (top) side of a metal slab and a vacuum region of ≈ 2 nm. The simulated supercell was thus composed of 344 C, 163 B, 163 N, and 532 Pt atoms. The lattice constant in the lateral plane was set according to the optimized value of free-standing graphene (0.2464 nm). The positions (x, y, z coordinates) of C, B, N atoms as well as z coordinates of the two topmost layers of the substrate were fully relaxed until forces became smaller than 0.2 eV nm⁻¹. The STM images were calculated using the Tersoff–Hamann formalism.^[72]

Supporting Information

Supporting Information is available from the Wiley Online Library or from the author.

Acknowledgements

Financial support by the Deutsche Forschungsgemeinschaft through Grant No. KR 2912/12-1 and KR 2912/17-1 is acknowledged. The North-German Supercomputing Alliance (HLRN) is acknowledged for providing computer time.

Open access funding enabled and organized by Projekt DEAL.

Conflict of Interest

The authors declare no conflict of interest.

Data Availability Statement

Research data are not shared.

Keywords

graphene, hexagonal boron nitride, inelastic electron tunneling spectroscopy, intercalation, metal, scanning tunneling microscopy

Received: May 11, 2021

Revised: June 17, 2021

Published online: July 26, 2021

- [1] R. Ribeiro-Palau, C. Zhang, K. Watanabe, T. Taniguchi, J. Hone, C. R. Dean, *Science* **2018**, 361, 690.
- [2] C. H. Lui, Z. Li, K. F. Mak, E. Cappelluti, T. F. Heinz, *Nat. Phys.* **2011**, 7, 944.
- [3] W. Bao, L. Jing, J. Velasco, Y. Lee, G. Liu, D. Tran, B. Standley, M. Aykol, S. B. Cronin, D. Smirnov, M. Koshino, E. McCann, M. Bockrath, C. N. Lau, *Nat. Phys.* **2011**, 7, 948.

- [4] T. Jiang, H. Liu, D. Huang, S. Zhang, Y. Li, X. Gong, Y.-R. Shen, W.-T. Liu, S. Wu, *Nat. Nanotechnol.* **2014**, 9, 825.
- [5] Y. Shan, Y. Li, D. Huang, Q. Tong, W. Yao, W.-T. Liu, S. Wu, *Sci. Adv.* **2018**, 4, eaat0074.
- [6] C. Gong, L. Li, Z. Li, H. Ji, A. Stern, Y. Xia, T. Cao, W. Bao, C. Wang, Y. Wang, Z. Q. Qiu, R. J. Cava, S. G. Louie, J. Xia, X. Zhang, *Nature* **2017**, 546, 265.
- [7] B. Huang, G. Clark, E. Navarro-Moratalla, D. R. Klein, R. Cheng, K. L. Seyler, D. Zhong, E. Schmidgall, M. A. McGuire, D. H. Cobden, W. Yao, D. Xiao, P. Jarillo-Herrero, X. Xu, *Nature* **2017**, 546, 270.
- [8] D. J. O'Hara, T. Zhu, A. H. Trout, A. S. Ahmed, Y. K. Luo, C. H. Lee, M. R. Brenner, S. Rajan, J. A. Gupta, D. W. McComb, R. K. Kawakami, *Nano Lett.* **2018**, 18, 3125.
- [9] M. Bonilla, S. Kolekar, Y. Ma, H. C. Diaz, V. Kalappattil, R. Das, T. Eggers, H. R. Gutierrez, M.-H. Phan, M. Batzill, *Nat. Nanotechnol.* **2018**, 13, 289.
- [10] W. Chen, Z. Sun, Z. Wang, L. Gu, X. Xu, S. Wu, C. Gao, *Science* **2019**, 366, 983.
- [11] C. R. Dean, A. F. Young, I. Meric, C. Lee, L. Wang, S. Sorgenfrei, K. Watanabe, T. Taniguchi, P. Kim, K. L. Shepard, J. Hone, *Nat. Nanotechnol.* **2010**, 5, 722.
- [12] C. Dean, A. Young, L. Wang, I. Meric, G.-H. Lee, K. Watanabe, T. Taniguchi, K. Shepard, P. Kim, J. Hone, *Solid State Commun.* **2012**, 152, 1275.
- [13] K. S. Novoselov, A. K. Geim, S. V. Morozov, D. Jiang, Y. Zhang, S. V. Dubonos, I. V. Grigorieva, A. A. Firsov, *Science* **2004**, 306, 666.
- [14] Y. Zhang, Y.-W. Tan, H. L. Stormer, P. Kim, *Nature* **2005**, 438, 201.
- [15] Y. Zhang, V. W. Brar, F. Wang, C. Girit, Y. Yayon, M. Panlasigui, A. Zettl, M. F. Crommie, *Nat. Phys.* **2008**, 4, 627.
- [16] E. Y. Andrei, G. Li, X. Du, *Rep. Prog. Phys.* **2012**, 75, 056501.
- [17] C. R. Dean, A. F. Young, P. Cadden-Zimansky, L. Wang, H. Ren, K. Watanabe, T. Taniguchi, P. Kim, J. Hone, K. L. Shepard, *Nat. Phys.* **2011**, 7, 693.
- [18] A. S. Mayorov, R. V. Gorbachev, S. V. Morozov, L. Britnell, R. Jalil, L. A. Ponomarenko, P. Blake, K. S. Novoselov, K. Watanabe, T. Taniguchi, A. K. Geim, *Nano Lett.* **2011**, 11, 2396.
- [19] S. J. Haigh, A. Gholinia, R. Jalil, S. Romani, L. Britnell, D. C. Elias, K. S. Novoselov, L. A. Ponomarenko, A. K. Geim, R. Gorbachev, *Nat. Mater.* **2012**, 11, 764.
- [20] A. Nagashima, Y. Gamou, M. Terai, M. Wakabayashi, C. Oshima, *Phys. Rev. B* **1996**, 54, 13491.
- [21] C. Oshima, A. Itoh, E. Rokuta, T. Tanaka, K. Yamashita, T. Sakurai, *Solid State Commun.* **2000**, 116, 37.
- [22] T. Kawasaki, T. Ichimura, H. Kishimoto, A. A. Akbar, T. Ogawa, C. Oshima, *Surf. Rev. Lett.* **2002**, 9, 1459.
- [23] C. Bjelkevig, Z. Mi, J. Xiao, P. A. Dowben, L. Wang, W.-N. Mei, J. A. Kelber, *J. Phys.: Condens. Matter* **2010**, 22, 302002.
- [24] Z. Liu, L. Song, S. Zhao, J. Huang, L. Ma, J. Zhang, J. Lou, P. M. Ajayan, *Nano Lett.* **2011**, 11, 2032.
- [25] S. Roth, F. Matsui, T. Greber, J. Osterwalder, *Nano Lett.* **2013**, 13, 2668.
- [26] S. Roth, T. Greber, J. Osterwalder, *ACS Nano* **2016**, 10, 11187.
- [27] D. Usachov, V. K. Adamchuk, D. Haberer, A. Grüneis, H. Sachdev, A. B. Preobrajenski, C. Laubschat, D. V. Vyalikh, *Phys. Rev. B* **2010**, 82, 075415.
- [28] W. Yang, G. Chen, Z. Shi, C.-C. Liu, L. Zhang, G. Xie, M. Cheng, D. Wang, R. Yang, D. Shi, K. Watanabe, T. Taniguchi, Y. Yao, Y. Zhang, G. Zhang, *Nat. Mater.* **2013**, 12, 792.
- [29] S. M. Kim, A. Hsu, P. T. Araujo, Y.-H. Lee, T. Palacios, M. Dresselhaus, J.-C. Idrobo, K. K. Kim, J. Kong, *Nano Lett.* **2013**, 13, 933.
- [30] J. Halle, A. Mehler, N. Néel, J. Kröger, *Phys. Chem. Chem. Phys.* **2019**, 21, 3140.
- [31] W. Auwärter, *Surf. Sci. Rep.* **2019**, 74, 1.
- [32] M. Paffett, R. Simonson, P. Papin, R. Paine, *Surf. Sci.* **1990**, 232, 286.

- [33] A. Nagashima, N. Tejima, Y. Gamou, T. Kawai, C. Oshima, *Phys. Rev. Lett.* **1995**, *75*, 3918.
- [34] W. Auwärter, M. Muntwiler, J. Osterwalder, T. Greber, *Surf. Sci.* **2003**, *545*, L735.
- [35] A. Preobrajenski, A. Vinogradov, N. Mårtensson, *Surf. Sci.* **2005**, *582*, 21.
- [36] M. Morscher, M. Corso, T. Greber, J. Osterwalder, *Surf. Sci.* **2006**, *600*, 3280.
- [37] T. Land, T. Michely, R. Behm, J. Hemminger, G. Comsa, *Surf. Sci.* **1992**, *264*, 261.
- [38] T. Fujita, W. Kobayashi, C. Oshima, *Surf. Interface Anal.* **2005**, *37*, 120.
- [39] Z. Liang, H. Khosravian, A. Uhl, R. J. Meyer, M. Trenary, *Surf. Sci.* **2012**, *606*, 1643.
- [40] A. Mehler, N. Néel, J. Kröger, *J. Vac. Sci. Technol., A* **2019**, *37*, 061404.
- [41] A. Mehler, N. Néel, J. Kröger, *J. Phys. Chem. Lett.* **2020**, *11*, 5204.
- [42] A. Goriachko, Y. B. He, H. Over, *J. Phys. Chem. C* **2008**, *112*, 8147.
- [43] Y. Pan, M. Gao, L. Huang, F. Liu, H.-J. Gao, *Appl. Phys. Lett.* **2009**, *95*, 093106.
- [44] R. Kunkel, B. Poelsema, L. K. Verheij, G. Comsa, *Phys. Rev. Lett.* **1990**, *65*, 733.
- [45] M. Bott, T. Michely, G. Comsa, *Surf. Sci.* **1992**, *272*, 161.
- [46] M. Gao, Y. Pan, L. Huang, H. Hu, L. Z. Zhang, H. M. Guo, S. X. Du, H.-J. Gao, *Appl. Phys. Lett.* **2011**, *98*, 033101.
- [47] A. B. Preobrajenski, M. L. Ng, A. S. Vinogradov, N. Mårtensson, *Phys. Rev. B* **2008**, *78*, 073401.
- [48] A. B. Preobrajenski, A. S. Vinogradov, M. L. Ng, E. Čavar, R. Westerström, A. Mikkelsen, E. Lundgren, N. Mårtensson, *Phys. Rev. B* **2007**, *75*, 245412.
- [49] V. W. Brar, Y. Zhang, Y. Yayon, T. Ohta, J. L. McChesney, A. Bostwick, E. Rotenberg, K. Horn, M. F. Crommie, *Appl. Phys. Lett.* **2007**, *91*, 122102.
- [50] V. W. Brar, S. Wickenburg, M. Panlasigui, C.-H. Park, T. O. Wehling, Y. Zhang, R. Decker, Ç. Girit, A. V. Balatsky, S. G. Louie, A. Zettl, M. F. Crommie, *Phys. Rev. Lett.* **2010**, *104*, 036805.
- [51] R. Decker, Y. Wang, V. W. Brar, W. Regan, H.-Z. Tsai, Q. Wu, W. Gannett, A. Zettl, M. F. Crommie, *Nano Lett.* **2011**, *11*, 2291.
- [52] F. D. Natterer, Y. Zhao, J. Wyrick, Y.-H. Chan, W.-Y. Ruan, M.-Y. Chou, K. Watanabe, T. Taniguchi, N. B. Zhitenev, J. A. Stroscio, *Phys. Rev. Lett.* **2015**, *114*, 245502.
- [53] H. W. Kim, W. Ko, J. Ku, I. Jeon, D. Kim, H. Kwon, Y. Oh, S. Ryu, Y. Kuk, S. W. Hwang, H. Suh, *Nat. Commun.* **2015**, *6*, 7528.
- [54] N. Néel, C. Steinke, T. O. Wehling, J. Kröger, *Phys. Rev. B* **2017**, *95*, 161410.
- [55] J. Halle, N. Néel, M. Fonin, M. Brandbyge, J. Kröger, *Nano Lett.* **2018**, *18*, 5697.
- [56] J. Kröger, N. Néel, T. O. Wehling, M. Brandbyge, *Small Methods* **2020**, *4*, 1900817.
- [57] A. Allard, L. Wirtz, *Nano Lett.* **2010**, *10*, 4335.
- [58] T. Aizawa, Y. Hwang, W. Hayami, R. Souda, S. Otani, Y. Ishizawa, *Surf. Sci.* **1992**, *260*, 311.
- [59] A. Politano, A. R. Marino, G. Chiarello, *J. Phys.: Condens. Matter* **2012**, *24*, 104025.
- [60] M. Endlich, A. Molina-Sánchez, L. Wirtz, J. Kröger, *Phys. Rev. B* **2013**, *88*, 205403.
- [61] A. A. Taleb, D. Farías, *J. Phys.: Condens. Matter* **2016**, *28*, 103005.
- [62] G. J. Slotman, G. A. de Wijs, A. Fasolino, M. I. Katsnelson, *Ann. Phys.* **2014**, *526*, 381.
- [63] S. Jung, M. Park, J. Park, T.-Y. Jeong, H.-J. Kim, K. Watanabe, T. Taniguchi, D. H. Ha, C. Hwang, Y.-S. Kim, *Sci. Rep.* **2015**, *5*, 16642.
- [64] G. S. N. Eliel, M. V. O. Moutinho, A. C. Gadelha, A. Righi, L. C. Campos, H. B. Ribeiro, P.-W. Chiu, K. Watanabe, T. Taniguchi, P. Puech, M. Paillet, T. Michel, P. Venezuela, M. A. Pimenta, *Nat. Commun.* **2018**, *9*, 1221.
- [65] H.-Q. Song, Z. Liu, D.-B. Zhang, *Phys. Lett. A* **2019**, *383*, 2628.
- [66] I. Horcas, R. Fernández, J. M. Gómez-Rodríguez, J. Colchero, J. Gómez-Herrero, A. M. Baro, *Rev. Sci. Instrum.* **2007**, *78*, 013705.
- [67] G. Kresse, J. Hafner, *J. Phys.: Condens. Matter* **1994**, *6*, 8245.
- [68] G. Kresse, J. Furthmüller, *Phys. Rev. B* **1996**, *54*, 11169.
- [69] J. P. Perdew, K. Burke, M. Ernzerhof, *Phys. Rev. Lett.* **1996**, *77*, 3865.
- [70] P. E. Blöchl, *Phys. Rev. B* **1994**, *50*, 17953.
- [71] S. Grimme, *J. Comput. Chem.* **2006**, *27*, 1787.
- [72] J. Tersoff, D. R. Hamann, *Phys. Rev. B* **1985**, *31*, 805.